Journal of Catalysis **202,** 100–109 (2001)
doi:10.1006/jcat.2001.3247, available online at http://www.idealibrary.com on IDEAL®

Preparation and Characterisation of Bimetallic Cobalt and Molybdenum Carbides

Tian-Cun Xiao, Andrew P. E. York,[1] Hamid Al-Megren, Cliff V. Williams, Hai-Tao Wang,
and Malcolm L. H. Green[2]

Wolfson Catalysis Centre, Inorganic Chemistry Laboratory, University of Oxford, South Parks Road, Oxford OX1 3QR, United Kingdom

Received January 22, 2001; revised April 6, 2001; accepted April 6, 2001

A series of mixed metal oxides $Co_xMo_{1-x}O_y$ have been prepared by calcination of a mechanical mixture of $Co(NO_3)_2$ and molybdenum oxide. They were carburised by temperature-programmed reactions using a C_2H_6/H_2 gas mixture. The carburisation process was monitored with GC-MS. The catalytic performance of the resulting mixed metal carbide catalysts was evaluated for hydrodenitrogenation using pyridine as the model reactant. The oxide precursors and the catalysts have been characterized by X-ray diffraction (XRD), laser Raman spectrum, infrared spectrum, ^{13}C solid state NMR, and scanning electron microscope (SEM). The data show that addition of cobalt to molybdenum oxide leads to both $CoMoO_4$ and a new complex oxide phase. During the carburisation reaction, some oxides decompose and the initial cobalt oxide is first reduced to the metallic state, and this then catalyses the hydrogenolysis of ethane into methane, which further carburises molybdenum oxide. The presence of the cobalt oxide lowers the temperature required for the carburisation of pure molybdenum oxide. The $Co_{0.2}Mo_{0.8}C_x$ system is a homogeneous bimetallic carbide phase, but the $Co_{0.4}Mo_{0.6}C_x$ and $Co_{0.5}Mo_{0.5}C_x$ systems contain impurity phases of Co metal, Co_3C, and Mo_2C. NMR spectra reveal that the face-centred cubic (fcc) carbide (MoC_{1-x}) is the main phase present in the bimetallic carbide. The shape of the carbide particles become more regular as the Co content increases. Catalytic stability under hydrodenitrogenation conditions increases from $Co_{0.2}Mo_{0.8}C_x$ to $Co_{0.4}Mo_{0.6}C_x$. However, when the Co content is increased to 0.5, the lifetime of the catalyst for pyridine HDN is greatly decreased and the surface symmetry of the carbide changes during the reaction.

Key Words: **CoMo bimetallic carbides; XRD; NMR; HDN.**

INTRODUCTION

Levy and Boudart (1) developed the TPRe method for the preparation of high surface area carbides and found a similarity between early transition metal carbides and noble metal catalysts. These carbide materials have been extensively studied as alternative catalysts to precious metals (2, 3). Transition metal carbide catalysts have shown much higher activity for hydrogen transfer reactions (4–23), especially for hydrodenitrogenation (14, 17, 19–21). In some cases, they show superior selectivity, stability, and resistance to poisoning (11, 24). Addition of a second metal can modify the structure and catalytic performance of the resulting bimetallic carbides. Oyama and co-workers (20, 22) pointed out that a Co–Mo–O–N system has the highest known HDS activity, while Nb–Mo–O–C material shows higher HDN activity than the commercial NiMo sulfide catalyst. However, little work has been done on the effect of cobalt additives on the structure and activity of molybdenum carbide catalysts (25), although the presence of Co in the HDS catalysts gives rise to synergistic effects on catalytic activity (26–28). In this work, we described a series of cobalt–molybdenum bimetallic carbides and the effect of cobalt additives on the structure and performance of the cobalt–molybdenum carbide catalysts.

EXPERIMENTAL

A series of mixed CoMo oxide samples was prepared. Cobalt nitrate was mechanically mixed with molybdenum trioxide (Alfa, >99.995%) at Co/Mo atomic ratios of 0.25, 0.5, 0.67, and 1.0, respectively. Ethanol (10 cm^3) was added to each mixture with stirring. A slurry was obtained, and solvent was removed gradually while stirring was continued. The dried powder was then thoroughly mixed for 2 h using a pestle and mortar and then calcined at 873 K in air for 3 h. It was cooled to room temperature and ground into a fine powder. To increase uniformity, the powder was pressed into a pellet, which was placed in a furnace and calcined in air at 873 K for 24 h. The pellets were cooled to room temperature, then crushed, and sieved to smaller than 250 μm. The resulting powder samples are labeled as $Co_{0.2}Mo_{0.8}O_x$, $Co_{0.33}Mo_{0.67}O_x$, $Co_{0.4}Mo_{0.6}O_x$, and $Co_{0.5}Mo_{0.5}O_x$ corresponding to the calculated Co/Mo ratios of 0.25, 0.5, 0.67, and 1.0, respectively.

In a typical experiment, CoMo bimetallic oxide powder was treated by temperature-programmed reduction in a

---

[1] Current address: Johnson Matthey Technological Centre, Blount's Court, Sonning Common, Reading RG4 9NH, U.K.

[2] To whom correspondence should be addressed. Fax: +44-1865-272690. E-mail: malcolm.green@chem.ox.ac.uk.

0021-9517/01 $35.00

flow of 10 vol% C_2H_6 (purity >99.95%) in H_2 (total flow = 100 cm^3/min) at a rate of 1 K/min up to 900 K. The reduction was continued at this temperature for ca. 2 h until no carbon oxides could be detected in the exhausted gas. A GC-MS (Hewlett-Packard 5890A gas chromatograph fitted with a Hewlett-Packard 5791A quadrupole mass spectrometer detector (MS)) was employed to analyse the gas products during the carburisation process. The mass range of m/e 10–100 was scanned at 1-s intervals, which allowed the gases of CO, CO_2, H_2O, CH_4, C_2H_4, and C_2H_6 to be monitored by their parent ions. In each experiment, 1.2 g of a CoMo oxide was loaded into a commercial Labcon quartz microreactor (o.d. 10 mm) with quartz wool at the two ends to maintain the powder. After the carburisation process, the sample was quenched to room temperature under Ar by removing the tube from the furnace. Before exposure to the atmosphere, the samples were passivated in flowing 1.0 vol% O_2/Ar.

The structure and components of the mixed oxide and carburised materials were studied by X-ray diffraction (XRD) using a Philips PW1710 diffractometer with Cu$K\alpha$ radiation. The bimetallic CoMo oxide samples were mounted on an aluminum plate with a groove cut into it and smoothed using a microscope slide, while the carbides were mounted on a glass slide to avoid the aluminum diffraction, which can be confused with cobalt metal and cobalt carbides. Carbon content in the samples was determined by microanalysis, and the specific surface area of the CoMo carbides was measured on an ASAP 2010 (Micrometrics Instrument Corp.) using the N_2 adsorption method.

The morphology of the passivated samples was observed using scanning electron microscopy (SEM) on a Hitachi S-520 microscope operating at 20 kV and 40 mA. The powder sample was dispersed on the specimen holder with acetone.

^{13}C solid state MAS NMR measurements were carried out in a CMX-200 NMR spectrometer at a frequency of 50.31 MHz. The detailed measurement method has been described elsewhere (29). Typically, 20,000 scans were accumulated using a single pulse (45°), with a pulse delay of 1.0 s and a 4 kHz/s spinning speed. The spectra were recorded at room temperature using adamantane (δ = 29.5) as the reference.

Raman spectra were recorded in air with a resolution of 2 cm^{-1} using a Yvon Jobin Labram spectrometer with a 632-nm HeNe laser, run in a back-scattered confocal arrangement. The samples were pressed in a microscope slide; the scanning time was set to 60 s. The scanning range was 90 to 3000 cm^{-1}.

The activity of the bimetallic carbide was evaluated using pyridine HDN as the model reaction. Carbide catalyst (0.2 g) was loaded into a 6-mm (o.d) silica tube and pretreated under flowing H_2 (20 ml/min) to 723 K for 4 h to remove the surface oxygen species. The catalyst was then cooled to reaction temperature. The inlet gas was switched to H_2 saturated with pyridine (273 K) at a flow rate of 20 ml/min. The pyridine concentration in the hydrogen was 6500 ppm, and the reaction pressure was 1 bar. The detailed procedure has been presented elsewhere (24). After the activity test, the catalyst was cooled to room temperature under flowing hydrogen and passivated by static exposure to air for 24 h before unloading.

RESULTS AND DISCUSSION

Study of the Structures of the Bimetallic Oxides

The XRD patterns of the bimetallic oxide samples are given in Fig. 1. The addition of cobalt to the molybdenum oxide gives rise to new X-ray diffraction peaks at 2θ of 14.5°, 27.3°, and 28.2°. These can be ascribed to the Scheelite-like structure of $CoMoO_4$ in a monoclinic phase. The mixed oxide $CoMoO_4$ has two crystal phases (30): one is stable at high temperatures and another at a lower temperature, but both phases can exist at room temperature. In our XRD patterns, the phases of $CoMoO_4$ are detected, and as the cobalt content increases, the diffraction peaks become more intense compared to the diffraction peaks of MoO_3. This suggests that increasingly $CoMoO_4$ is being formed in the bimetallic oxide. Meanwhile, diffraction peaks corresponding to MoO_3 become weaker. When the Co/Mo ratio is increased to 1, the diffraction peaks of MoO_3 have almost completely disappeared, and the prevailing diffraction peaks are due to the formation of $CoMoO_4$. Also, there are weak diffraction peaks corresponding to a small amount of a Co_3O_4 phase. When cobalt nitrate was treated by the

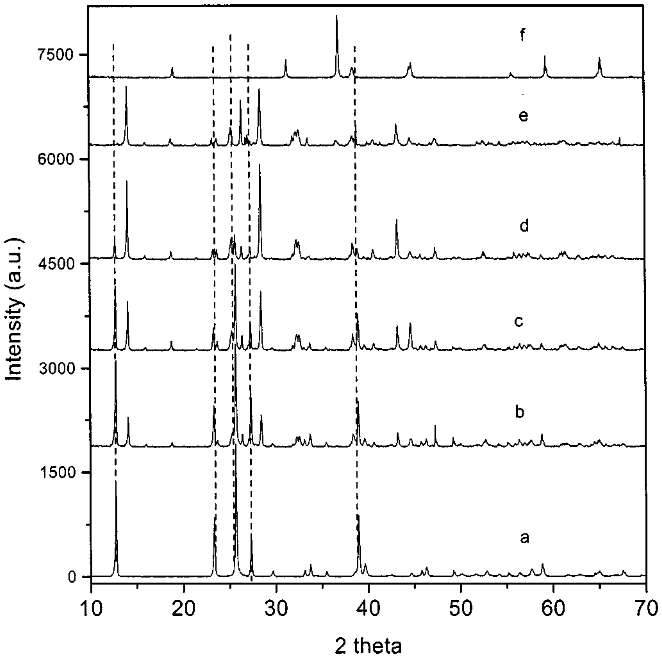

FIG. 1. XRD patterns of the bimetallic oxides.

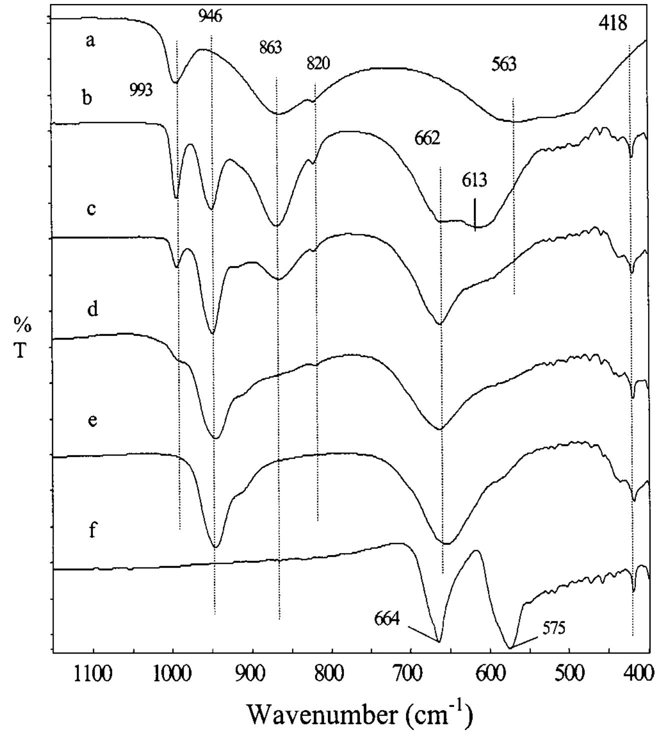

FIG. 2. IR spectra of (a) MoO_3, (b) $Co_{0.2}Mo_{0.8}O_x$, (c) $Co_{0.33}Mo_{0.67}O_x$, (d) $Co_{0.4}Mo_{0.6}O_x$, (e) $Co_{0.5}Mo_{0.5}O_x$, and (f) Co_3O_4.

same procedure used for the bimetallic oxides, then Co_3O_4 is formed.

The infrared spectra of the bimetallic oxides are shown in Fig. 2. For the pure MoO_3, the main bands occur at 993, 863, 820, and 563 cm^{-1}, which can be assigned to Mo=O stretching and Mo–O–Mo bending vibrations. The IR spectrum of $Co_{0.2}Mo_{0.8}O_x$ (Fig. 2b) shows the presence of MoO_3 and new bands at 946 and 662 cm^{-1}, which can be assigned to asymmetric νMo=O stretching modes of the MoO_4 tetrahedral units (31). The IR peaks due to MoO_3 become weaker, while those of the MoO_4 tetrahedral become more intense with increasing Co content in the samples. The IR spectra of $Co_{0.4}Mo_{0.6}O_x$ and $Co_{0.5}Mo_{0.5}O_x$ contain mainly the vibrations of the MoO_4 units, and the bands due to MoO_3 are absent. Bands associated with the Co_3O_4 oxides (664 and 575 cm^{-1}) are very weak and almost submerged into the bands of the MoO_4 units; hence, it is difficult to determine the presence of Co_3O_4 using an IR spectroscope.

The Raman spectra of the CoMo bimetallic oxides samples (Fig. 3) suggest that the main phase in the surface of $Co_{0.2}Mo_{0.8}O_x$ is MoO_3 (Fig. 3b), although IR and XRD data suggest that $CoMoO_4$ is present. The main Raman bands at 994, 819, and 290 cm^{-1} correspond to the antisymmetric stretching mode of Mo–O–Mo, the stretching mode of Mo=O, and the bending mode of the Mo=O group in polycrystalline MoO_3, respectively (32). The weak band at 941.7 cm^{-1} is due to the A_1 mode of Mo=O in the MoO_4 tetrahedral unit. The $Co_{0.33}Mo_{0.67}O_x$ sample shows a broad band at 941.7 cm^{-1}, which increases in intensity and can be resolved into two peaks. These bands are characteristic for $CoMoO_4$. However, the Raman bands due to MoO_3 are still quite strong in this sample, suggesting that the main phase present on the surface of this sample is MoO_3. When the Co/Mo ratio is increased to 0.67 and 1.0, the Raman bands of MoO_3 are weaker until they almost disappear. Meanwhile, the bands at 819, 884, and 941.7 cm^{-1} increase in intensity. This suggests that the main phase on the surface of $Co_{0.4}Mo_{0.6}O_x$ and $Co_{0.5}Mo_{0.5}O_x$ is β-$CoMoO_4$ (33). It is also seen from Fig. 3 that no Raman bands corresponding to Co_3O_4 exist in the spectrum of the CoMo bimetallic oxides.

TPRe-MS Results of Carburisation of the CoMo Bimetallic Oxides

The product distribution during carburisation of the Co and Mo bimetallic oxide samples with the mixture of ethane and hydrogen is shown in Figs. 4–7. Water ($m/e = 18$) starts to form at 666, 613, 596, and 583 K for $Co_{0.2}Mo_{0.8}O_x$, $Co_{0.33}Mo_{0.67}O_x$, $Co_{0.4}Mo_{0.6}O_x$, and $Co_{0.5}Mo_{0.5}O_x$, respectively. For $Co_{0.2}Mo_{0.8}O_x$, water starts to form while no changes are seen for ethane ($m/e = 30$, 28); this suggests that hydrogen takes part in the first reduction of the oxide. However, in the carburisation process of the other three Co and Mo bimetallic oxide samples, the water formation commences at the same time that methane is formed, and ethane is consumed. This indicates that with these samples the water resulted from the reduction of the $CoMoO_4$ by

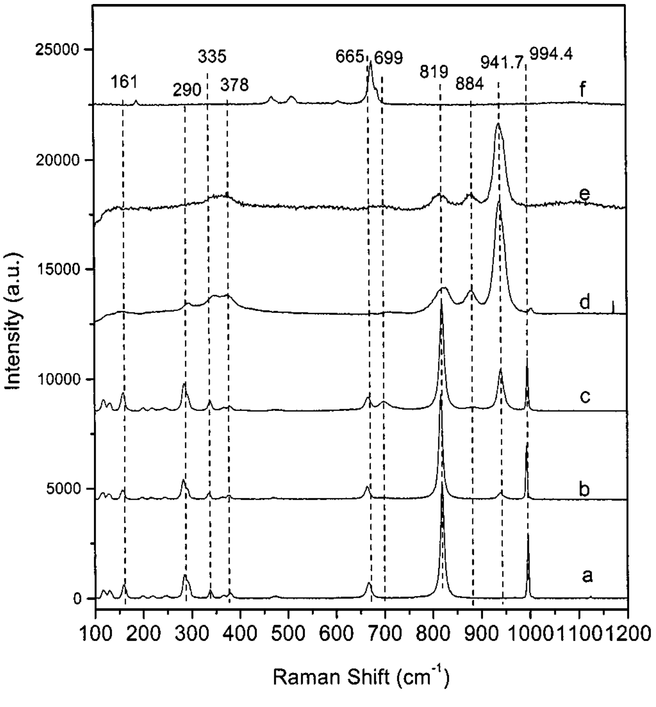

FIG. 3. Laser Raman spectra of (a) MoO_3, (b) $Co_{0.2}Mo_{0.8}O_x$, (c) $Co_{0.33}Mo_{0.67}O_x$, (d) $Co_{0.4}Mo_{0.6}O_x$, (e) $Co_{0.5}Mo_{0.5}O_x$, and (f) Co_3O_4.

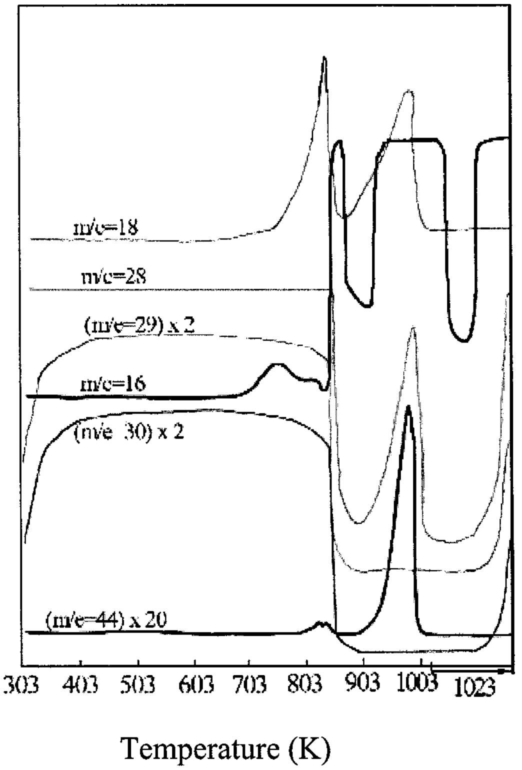

FIG. 4. TPRe-MS of $Co_{0.2}Mo_{0.8}O_x$ using 10% C_2H_6 balanced with hydrogen.

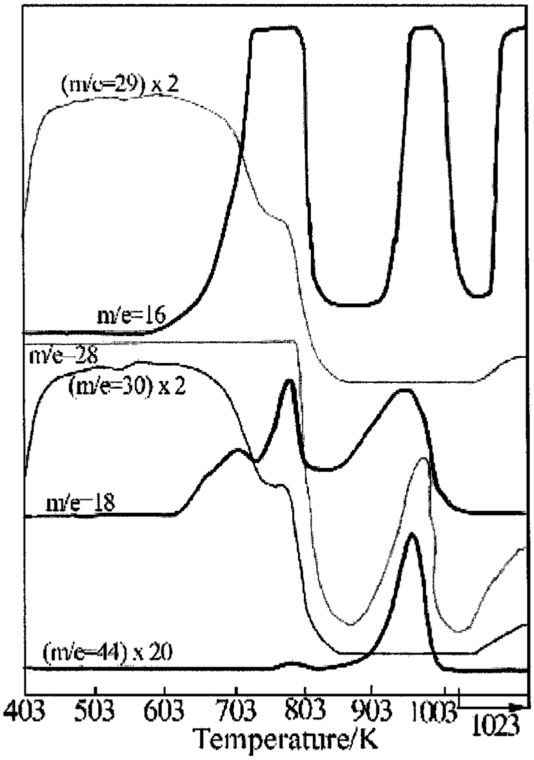

FIG. 6. TPRe-MS of $Co_{0.4}Mo_{0.6}O_x$ using 10% C_2H_6 balanced with hydrogen.

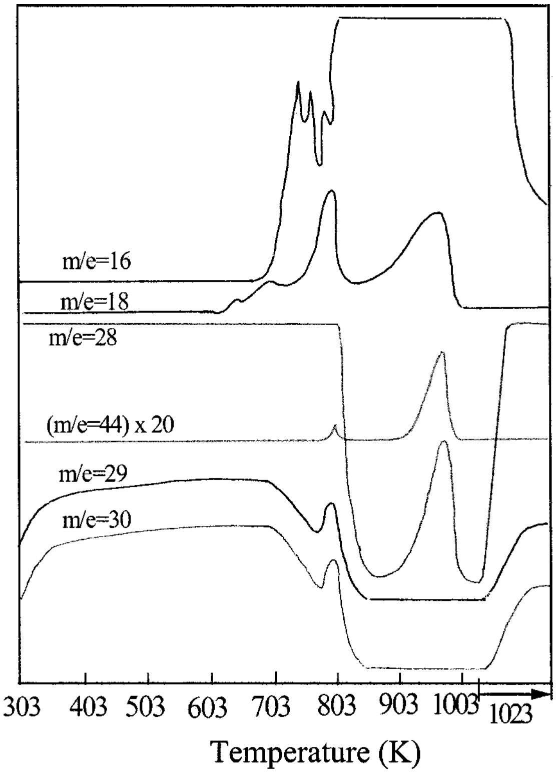

FIG. 5. TPRe-MS of $Co_{0.33}Mo_{0.67}O_x$ using 10% C_2H_6 balanced with hydrogen.

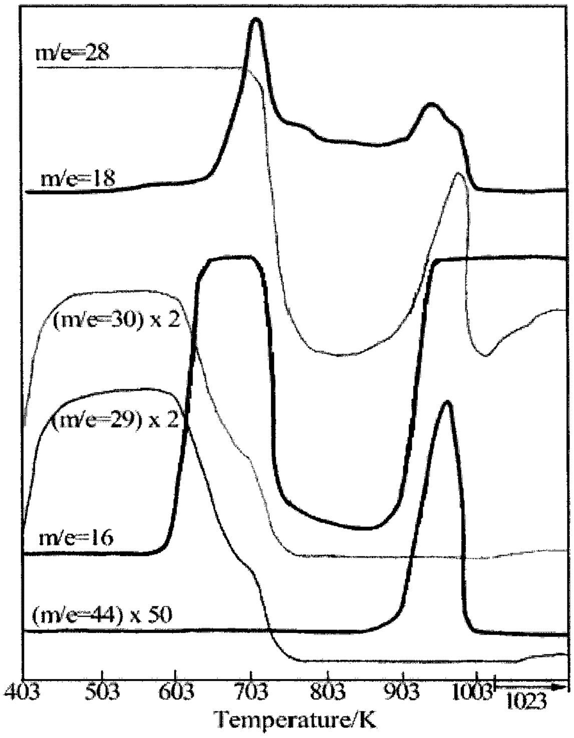

FIG. 7. TPRe-MS of $Co_{0.5}Mo_{0.5}O_x$ using 10% C_2H_6 balanced with hydrogen.

both hydrogen and ethane. A comparison of the carburisation processes of MoO_3 and Co–Mo oxides reveals that the temperatures of water formation and ethane hydrogenolysis in the Co–Mo system are much lower than those for pure molybdenum trioxide (34). Also, the temperatures decrease with increasing cobalt content in the bimetallic oxide samples.

Ethane concentration in the exhaust gas starts to decrease at 825, 708, 653, and 603 K for $Co_{0.2}Mo_{0.8}O_x$, $Co_{0.33}Mo_{0.67}O_x$, $Co_{0.4}Mo_{0.6}O_x$, and $Co_{0.5}Mo_{0.5}O_x$, respectively. This suggests that ethane becomes more active in the carburisation as the Co content increases in the starting bimetallic oxides. During the carburisation of $Co_{0.33}Mo_{0.67}O_x$, $Co_{0.4}Mo_{0.6}O_x$, and $Co_{0.5}Mo_{0.5}O_x$, the quantity of ethane in the carburising agent decreases initially, then increases, and finally continuously decreases to almost zero. This suggests that ethane initially reacts with the partially reduced CoMo oxides and changes it to an oxy-carbide. This oxy-carbide is inactive for catalysing the hydrogenolysis of ethane. As the temperature increases, the oxy-carbide becomes an active catalyst for the hydrogenolysis of ethane, and the ethane is completely converted into methane. When the oxide is carburised at 1023 K, the surface becomes covered with carbon and ethane appears again.

Two peaks due to the formation of CO_2 ($m/e = 44$) are seen at 804 and 963 K during carburisation of $Co_{0.2}Mo_{0.8}O_x$, $Co_{0.33}Mo_{0.67}O_x$, and $Co_{0.4}Mo_{0.6}O_x$, and they correspond to the maximum of water production. The peak at 804 K is due to the reduction of molybdenum oxide by ethane, and the one at 963 K comes from the carburisation of the partially reduced bimetallic oxide with the methane produced from the hydrogenolysis of ethane. The peaks due to CO_2 production do not change with cobalt content in the starting oxide. This shows that the CO_2 production is probably related only to the carburisation of molybdenum oxide. Only one CO_2 production peak is seen in the carburisation of $Co_{0.5}Mo_{0.5}O_x$ at 963 K. This is because no excess of MoO_3 is present in the samples.

The XRD patterns of the carburised samples are given in Fig. 8. The overall diffraction patterns are different from those of the oxide precursors. The diffraction peak intensity of the bimetallic carbides becomes much weaker than that of the monometallic molybdenum carbides. This suggests that the particle size of the CoMo bimetallic carbide is smaller than that of pure molybdenum carbide. The diffraction pattern of $Co_{0.2}Mo_{0.8}C_x$ is similar to that of Mo_2C; however, the half-height peak width becomes broader, and the diffraction peaks shift to a high diffraction angle. No pure cobalt metal or carbide is found in the material. This shows that the cobalt in $Co_{0.2}Mo_{0.8}C_x$ is present in the lattice of the molybdenum carbide. Because the radius of Co is smaller than Mo, Mo_2C carbide with partially substituted Co has a smaller cell size, and thus the diffraction peaks move downward. Further evidence for the cobalt being in the framework of molybdenum carbide is that Co exists in the form of $CoMoO_4$ in the oxide precursor. It has been shown that the carburisation of MoO_3 with ethane to carbide is a topotactical process (34). The orientation and the main framework of $CoMoO_4$ is not changed during the carburisation. Therefore, it is proposed that the Co is incorporated into the lattice of molybdenum carbide.

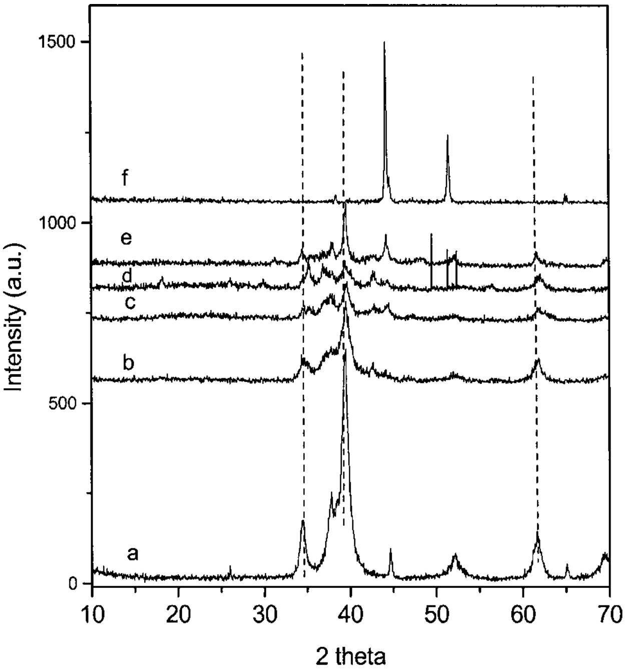

FIG. 8. XRD patterns of the cobalt and molybdenum carbides, (a) Mo_2C, (b) $Co_{0.2}Mo_{0.8}C_x$, (c) $Co_{0.33}Mo_{0.67}C_x$, (d) $Co_{0.4}Mo_{0.6}C_x$, (e) $Co_{0.5}Mo_{0.5}C_x$ and (f) Co_xC.

Figure 8c shows the XRD pattern of the $Co_{0.33}Mo_{0.67}C_x$ sample. The amount of pure molybdenum carbide has decreased because of the lower molybdenum oxide content in the calcined sample. The peaks at 2θ of 34.2°, 38.4°, and 43.2° increase; some of these peaks have been ascribed to the diffraction of aluminium (24). However, in this work, the XRD measurement was carried out using a microscope glass slide as the sample supporting plate, which has no diffraction peaks in this region. Therefore, these peaks can be assigned to a new phase of bimetallic carbide. When combined with the XRD results of $Co_{0.2}Mo_{0.8}C_x$ and the oxide precursors, these peaks are tentatively assigned to the diffraction of CoMo bimetallic carbide with an *eta*-type molybdenum carbide structure (35). When the Co/Mo ratio rises to 0.67, the peaks corresponding to the proposed CoMo bimetallic carbide become more intense, suggesting that more CoMo bimetallic carbide is formed. When the Co/Mo ratio is increased to 1.0, a strong peak at 2θ of 44.7° appears, which is from the X-ray diffraction of cobalt

TABLE 1

Carbon Content and Surface Area of the Cobalt and Molybdenum Carbides

Sample	Carbon content (wt%)	Surface (m^2/g)
$Co_{0.2}Mo_{0.8}C_x$	3.59	23.7
$Co_{0.33}Mo_{0.67}C_x$	2.73	27.2
$Co_{0.4}Mo_{0.6}C_x$	2.56	39.6
$Co_{0.5}Mo_{0.5}C_x$	2.73	15.5

metal; the other main diffraction peaks correspond to the molybdenum carbides. This result is different from the CoMo bimetallic nitride system in which a uniform Co–Mo–N_x is formed during the nitridation (36). However, carburisation of $CoMoO_4$ gives rise to Co metal and Mo_2C in the products, suggesting that phase separation occurs. Figure 8f shows the XRD pattern of the carburised cobalt oxide. It is seen that a small amount of cobalt carbide exists, although the main phase present is cobalt metal.

Elemental analysis and surface area measurement data are shown in Table 1. The carbon content decreases with the increase of cobalt to molybdenum ratio for samples of $Co_{0.2}Mo_{0.8}C_x$, $Co_{0.33}Mo_{0.67}C_x$, and $Co_{0.4}Mo_{0.6}C_x$. Hence, it is inferred that carbon in the bimetallic carbide arises mainly from the molybdenum carbide. The sample of $Co_{0.4}Mo_{0.6}C_x$ has the lowest carbon content, only 2.56 wt%, and the carbon content increases to 2.73 wt% in $Co_{0.5}Mo_{0.5}C_x$. This is probably because of the different carburisation process in which more graphic carbon is deposited on the $Co_{0.5}Mo_{0.5}C_x$.

The surface areas of the four Co and Mo bimetallic carbide samples are shown in Table 1. The surface areas of $Co_{0.2}Mo_{0.8}C_x$, $Co_{0.33}Mo_{0.67}C_x$, and $Co_{0.4}Mo_{0.6}C_x$ are 23.7, 27.2, and 39.6 m^2/g, respectively, although the carbon content in the three samples decreases gradually. This is probably because the cobalt–molybdenum bimetallic carbide is the main contribution to the surface area of the samples. In addition, the particle size becomes smaller with increasing Co content, which also would increase the surface area of the samples. $Co_{0.5}Mo_{0.5}C_x$ has the smallest surface area probably because of the phase separation, and the cobalt is present mainly as cobalt metal, which makes only a small contribution to the surface area.

Laser Raman data for the Co and Mo carbides are presented in Fig. 9. The laser Raman spectrum of Mo_2C is very similar to that of the molybdenum oxide precursor, (Fig. 3a) except for the vibration frequency shift from 994 and 819 cm^{-1} to 1006 and 828 cm^{-1} for the stretching vibration of Mo=O and Mo–O–Mo. The higher vibration frequency may be due to the partial replacement of oxygen by carbon. This result reflects the presence of Mo=O species over the carbide surface due to the passivation of the samples. The Raman spectrum of $Co_{0.2}Mo_{0.8}C_x$ shows weak bands of MoO_3 (1006 and 828 cm^{-1}) and strong bands of MoO_4 tetrahedra of $CoMoO_4$. The Raman bands of MoO_4 tetrahedra in $Co_{0.2}Mo_{0.8}C_x$ being stronger than those in $Co_{0.2}Mo_{0.8}O_x$ suggests that more $CoMoO_4$ is formed during the carburisation and passivation in the $Co_{0.2}Mo_{0.8}C_x$ sample.

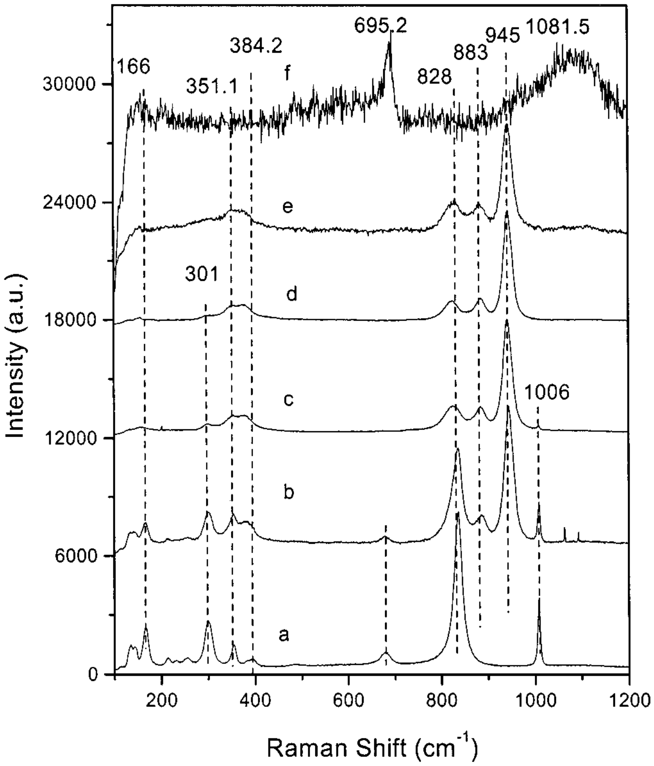

FIG. 9. Laser Raman spectra of (a) Mo_2C, (b) $Co_{0.2}Mo_{0.8}C_x$, (c) $Co_{0.33}Mo_{0.67}C_x$, (d) $Co_{0.4}Mo_{0.6}C_x$, (e) $Co_{0.5}Mo_{0.5}C_x$, and (f) Co_xC.

The Raman spectrum of $Co_{0.33}Mo_{0.67}C_x$ shows characteristic bands of MoO_4 tetrahedra, suggesting that, during the carburisation, all the bimetallic phases moved to the surface of the sample and covered the molybdenum carbide. After passivation, the bimetallic carbide is converted to $CoMoO_4$ and exists on the surface of the sample. The Raman mode of $Co_{0.4}Mo_{0.6}C_x$ is similar to its oxide precursor. The Raman bands of $Co_{0.5}Mo_{0.5}C_x$ are almost the same as those of $Co_{0.4}Mo_{0.6}C_x$, but the bands are weaker than the other samples, revealing that there is less $CoMoO_4$ present in the surface of this materials, because of the phase separation during the carbursation. The Raman spectrum of the pure carburised cobalt sample is shown in Fig. 10f. Two bands are observed at 695.2 and 1081.5 cm^{-1}, respectively, and the vibration mode is totally different from the CoMo bimetallic samples. This suggests that the structure of the CoMo bimetallic carbide is different from that of the pure carburised cobalt sample.

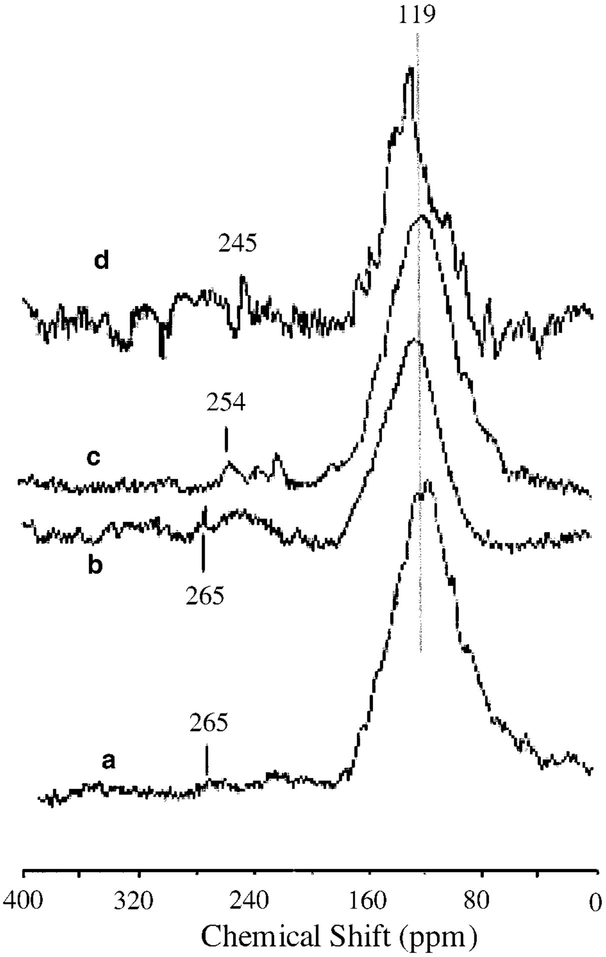

FIG. 10. ^{13}C NMR spectra of (a) $Co_{0.2}Mo_{0.8}C_x$, (b) $Co_{0.33}Mo_{0.67}C_x$, (c) $Co_{0.4}Mo_{0.6}C_x$, and (d) $Co_{0.5}Mo_{0.5}C_x$.

The ^{13}C MAS NMR spectra of $Co_{0.2}Mo_{0.8}C_x$, $Co_{0.33}Mo_{0.67}C_x$, $Co_{0.4}Mo_{0.6}C_x$, and $Co_{0.5}Mo_{0.5}C_x$ are given in Fig. 10; all samples show a main peak at 119 ppm; this band can be assigned to the resonance of carbon in molybdenum carbide with a fcc structure (29) or in eta-molybdenum carbide (MoC_{1-x}). A band at a higher chemical shift may be due to the incorporation of cobalt in the lattice of molybdenum carbide. A very small peak at about 275 ppm appears in $Co_{0.2}Mo_{0.8}C_x$ and $Co_{0.33}Mo_{0.67}C_x$ and shifts to 260 ppm in $Co_{0.4}Mo_{0.6}C_x$, and 250 ppm in $Co_{0.5}Mo_{0.5}C_x$, and the peaks increase in intensity with an increase of percentage of Co. This peak has been ascribed to the carbon in the lattice of hexagonal closed-packed molybdenum carbide (29). This suggests that there is a small quantity of Mo_2C present in the bimetallic carbide. The ^{13}C NMR spectrum of $Co_{0.5}Mo_{0.5}C_x$ has a poor signal-to-noise ratio, which may be due to the strong metallic property of the material. However, the main ^{13}C NMR peak shifts to 122 ppm, which is tentatively assigned to the bimetallic Co–Mo carbide.

The morphology of the bimetallic carbide samples has been studied using SEM, and morphologies are shown in Fig. 11. The particles of $Co_{0.2}Mo_{0.8}C_x$ are quite small, being about 2–3 μm with an irregular shape, and they are similar to the molybdenum carbide. This is to be expected since the main phase has the molybdenum carbide structure. For $Co_{0.33}Mo_{0.67}C_x$, the particle size grows to about 3–4 μm, still having an irregular shape. However, there is also considerable aggregation of other small particles, which may be a mixture of $CoMoC_x$ with molybdenum carbides. For $Co_{0.4}Mo_{0.6}C_x$, the morphology becomes regular and the size is about 5 μm, suggesting the phase in this sample is becoming more uniform. This observation coincides with the results of XRD and Raman spectra. For $Co_{0.5}Mo_{0.5}C_x$, the particle size has increased to 15–20 μm. However, the shape has become irregular and the surface of the crystals appears rough. This may reflect the occurrence of phase separation during the carburisation, giving a mixture of cobalt metal and molybdenum carbide.

The bimetallic carburised Co–Mo catalysts have been tested for their activity toward HDN using pyridine as the model compound; the results were presented elsewhere (24). They showed that nitrogen in pyridine was removed completely at 380°C and atmospheric pressure for all four catalysts, and the reaction temperature for complete removal of nitrogen from pyridine over the Co–Mo bimetallic carbide catalysts is lower than that for pure molybdenum carbide. This suggests that all the bimetallic catalysts were more stable and active than pure molybdenum carbide. The lifetime of the CoMo bimetallic carbide catalysts increases for the Co/Mo ratio from 0.25 to 0.67, and $Co_{0.4}Mo_{0.6}C_x$ possesses the highest stability, but the stability of $Co_{0.5}Mo_{0.5}C_x$ was almost the same as that of $Co_{0.2}Mo_{0.8}C_x$. The activity trends can be related to the structures of the samples. The XRD, Raman, and SEM show $Co_{0.4}Mo_{0.6}C_x$ has uniform particles of CoMo bimetallic carbide and thus is probably the more active component than Mo monometallic carbide for the HDN reaction.

The XRD data of the four CoMo carbides after HDN treatment are shown in Fig. 12, and they are similar to the initial samples as shown in Fig. 8. It appears that the structures of the carbides are maintained during the reaction. However, in the $Co_{0.5}Mo_{0.5}C_x$ sample, these peaks did not appear, but the diffraction peaks of the molybdenum carbide component have become sharper. It may be that particle aggregation has occurred during the reaction. These results suggest that the active phase in pyridine HDN reaction is the $CoMoC_x$ bimetallic carbide.

The Co and Mo carbides after pyridine HDN reaction were measured using laser Raman and the results are presented in Fig. 13. Compared to Fig. 10, the band at Mo=O in MoO_3 and MoO_4 tetrahedra shifts from 883 and 828 to

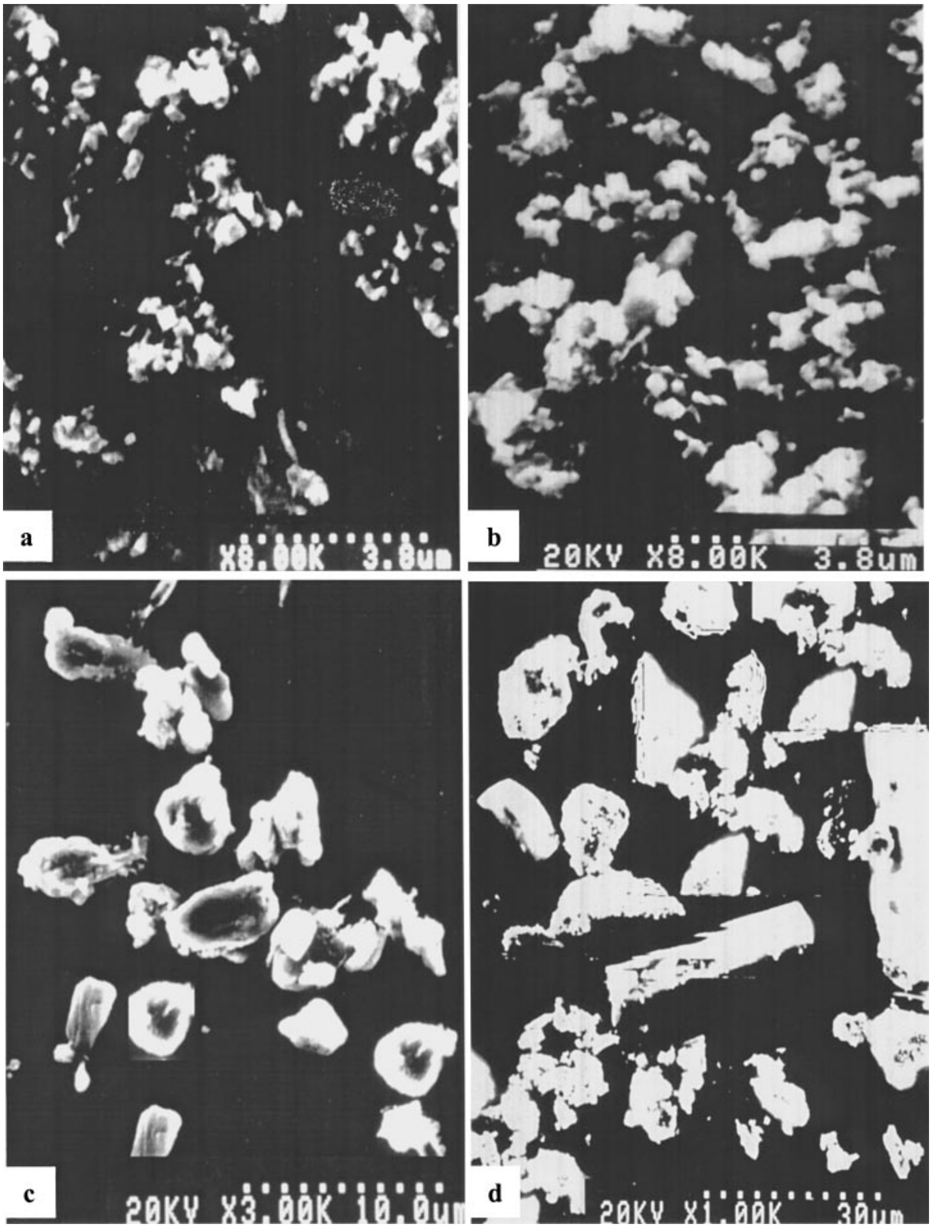

FIG. 11. SEM graphs of the as-prepared bimetallic carbides: (a) $Co_{0.2}Mo_{0.8}C_x$, (b) $Co_{0.33}Mo_{0.67}C_x$, (c) $Co_{0.4}Mo_{0.6}C_x$, and (d) $Co_{0.5}Mo_{0.5}C_x$.

891 and 833 cm^{-1} after reaction, suggesting the surface carbide is more stable and more oxygen is replaced by carbon after reaction. For the $Co_{0.2}Mo_{0.8}C_x$ sample, the peaks corresponding to the vibration of MoO_3 in the surface become weak, suggesting that surface molybdenum carbide can further interact with the $CoMoC_x$ and form more bimetallic carbide. This result coincides with XRD results in Fig. 13. In the case of $Co_{0.33}Mo_{0.67}C_x$, the Raman spectrum is almost unchanged, except two bands at 1118 and 687 cm^{-1} appear, which represents the existence of cobalt carbide in the materials. From this we can say that, during the reaction, a small amount of cobalt is separated from the $CoMoC_x$, which is probably the main reason for the decrease of the catalyst activity. However, no cobalt carbide is detected in the sample of $Co_{0.4}Mo_{0.6}C_x$ after the activity test, although more cobalt is contained in the $CoMoC_x$ bimetallic carbide. This is probably the reason why $Co_{0.4}Mo_{0.6}C_x$ is not deactivated after a 7-day run of pyridine HDN. Comparing Figs. 13a–c, it is also inferred that the stability of the $CoMoC_x$ is not only related to the Co content in the sample but also to the structure of the catalyst. More changes take place over $Co_{0.5}Mo_{0.5}C_x$ after the activity test. The Raman

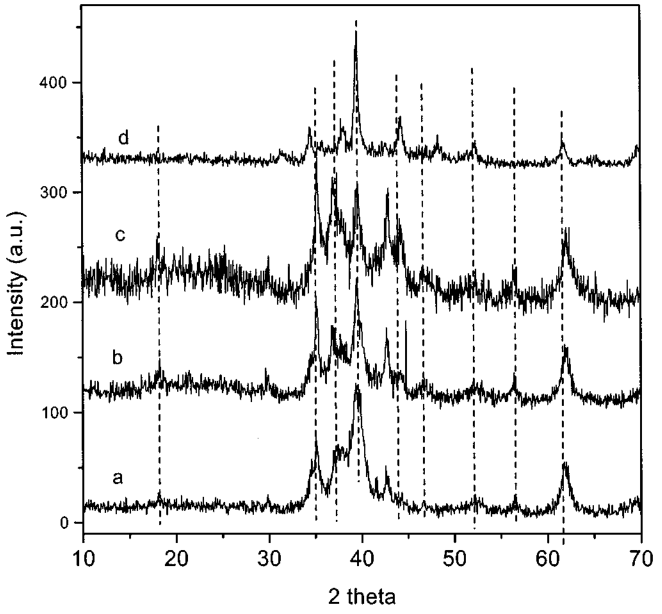

FIG. 12. XRD patterns of Co and Mo bimetallic carbides after pyridine HDN reaction: (a) $Co_{0.2}Mo_{0.8}C_x$, (b) $Co_{0.33}Mo_{0.67}C_x$, (c) $Co_{0.4}Mo_{0.6}C_x$, and (d) $Co_{0.5}Mo_{0.5}C_x$.

bands characteristic of $CoMoC_x$ further decrease in magnitude, and the main band at 945 cm^{-1} splits, which shows two kinds of $CoMoC_x$ exist in the samples. Meanwhile, the bands corresponding to cobalt carbide appear, suggesting that further phase separation occurs in this sample after reaction.

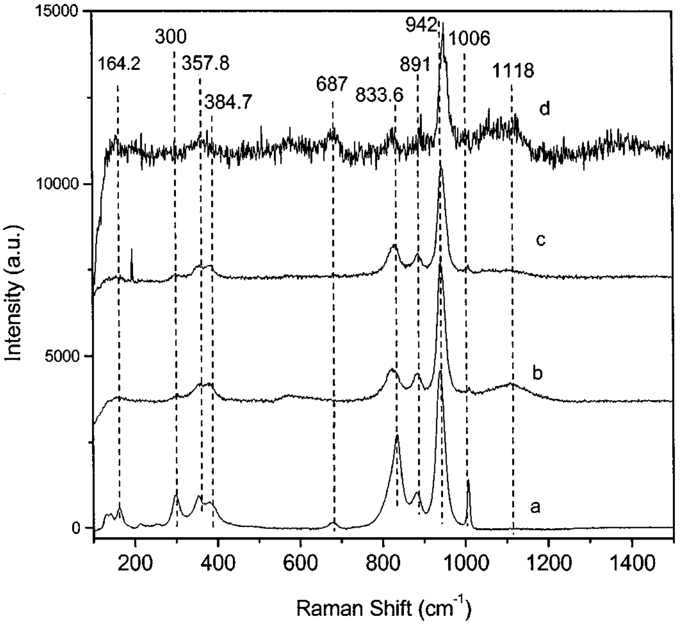

FIG. 13. Laser Raman spectra of Co and Mo bimetallic carbides after pyridine HDN reaction: (a) $Co_{0.2}Mo_{0.8}C_x$, (b) $Co_{0.33}Mo_{0.67}C_x$, (c) $Co_{0.4}Mo_{0.6}C_x$, and (d) $Co_{0.5}Mo_{0.5}C_x$.

CONCLUSIONS

Addition of cobalt nitrate to molybdenum trioxide followed by calcination of the mixture produced two different β-$CoMoO_4$ phases. During the carburisation using a mixture of hydrogen and ethane, the $Co_{0.2}Mo_{0.8}O_x$ first reacts with the hydrogen and then with ethane. The addition of cobalt appears to promote the activation of ethane during the carburisation process.

The particle size of the bimetallic carbide becomes smaller with an increase of Co content in the samples. The bimetallic carbide with eta-molybdenum carbide structure is present in $Co_{0.2}Mo_{0.8}C_x$, $Co_{0.33}Mo_{0.67}C_x$, and $Co_{0.4}Mo_{0.6}C_x$, but not in $Co_{0.5}Mo_{0.5}C_x$.

The XRD results show that the bulk phase of the carburised samples is carbide. Laser Raman spectra revealed that the surface of the passivated carbide is converted to oxide. The carburisation with ethane did not change the surface molecular symmetry. ^{13}C NMR results show that the cobalt and molybdenum carbide has an fcc structure.

The stability of the cobalt and molybdenum carbides in pyridine HDN increases from $Co_{0.2}Mo_{0.8}C_x$, $Co_{0.33}Mo_{0.67}C_x$, and $Co_{0.4}Mo_{0.6}C_x$. $Co_{0.5}Mo_{0.5}C_x$ has rather poor stability for the reaction. The more active component appears to be $CoMoC_x$; the deactivation of the catalyst results from the phase separation in the samples.

ACKNOWLEDGMENTS

Dr. Tiancun Xiao is a Royal Society BP-Amoco fellow from Shandong University, China. We thank CANMET and the GRI for financial support for A.P.E.York, King Abdulaziz City for Science and Technology for H. Al-Megren and to Colebrand Ltd. support for V. C. Williams. Thanks are due to Dr. Karl Coleman for the help in Raman measurements and fruitful discussion and to Dr. Nick Rees for NMR characterisation.

REFERENCES

1. Levy, R. B., and Boudart, M., *Science* **181**, 547 (1973).
2. Oyama, S. T., *Catal. Today* **15**, 179 (1992).
3. Chen, J. G., *Chem. Rev.* **96**, 1477 (1996).
4. Delannoy, L., Giraudon, J. M., Granger, P., Leclercq, L., and Leclercq, G., *Catal. Today* **59**, 231 (2000).
5. Chianelli, R. R., and Berhault, G., *Catal. Today* **53**, 357 (1999).
6. Gallo, P. D., Meunier, F., Pham-Huu, C., Crouzet, C., and Ledoux, J., *Ind. Eng. Chem. Res.* **36**, 4166 (1997).
7. Ranhotra, G. S., Bell, A. T., and Remer, J. A., *J. Catal.* **40**, 108 (1987).
8. Lee, J. S., Locatelli, S., Oyama, S. T., and Boudart, M., *J. Catal.* **125**, 157 (1990).
9. Lee, J. S., Yeom, M. H., Park, K. Y., Nam, I.-S., Chung, J. S., Kim, T. G., and Moon, S. H., *J. Catal.* **128**, 126 (1991).
10. Choi, J.-S., Bugli, G., and Djega-Mariadassou, G., *J. Catal.* **193**, 238 (2000).
11. Ledoux, M. J., Pham-Huu, C., Dunlop, H., and Guille, J., *J. Catal.* **134**, 383 (1992).
12. Ramanathan, S., and Oyama, S. T., *J. Phys. Chem.* **99**, 16365 (1995).
13. Choi, J-G., Brener, J. R., and Thompson, L. T., *J. Catal.* **154**, 33 (1995).
14. York, A. P. E., Claridge, J. B., Brungs, J., Tsang, S. C., and Green, M. L. H., *Chem. Commun.* **39** (1997).

15. Miyao, T., Oshikawa, K., Omi, S., and Nagai, M., *Stud. Surf. Sci. Catal.* **106**, 255 (1997).
16. Keller, V., Wehrer, P., Garin, F., Ducros, R., and Maire, G., *J. Catal.* **166**, 125 (1997).
17. Garin, F., Keller, V., Ducros, R., Muller, A., and Maire, G., *J. Catal.* **166**, 136 (1997).
18. Yu, C. C., Ramanathan, S., Dhandapani, B., Chen, J. G., and Oyama, S. T., *J. Phys. Chem. B* **101**, 512 (1997).
19. Claridge, J. B., York, A. P., Brungs, A. J., Marquez-Alvarez, C., Sloan, J., Tsang, S. C., and Green, M. L. H., *J. Catal.* **180**, 8 (1998).
20. Dhandapani, B., Ramanathan, S., Yu, C. C., Fruehberger, B., Chen, J. G., and Oyama, S. T., *J. Catal.* **176**, 61 (1998).
21. Neylon, M. K., Choi, S., Kwon, H., Curry, K. E., and Thompson, L. T., *Appl. Catal.* **183**, 253, 5 (1999).
22. Oyama, S. T., Yu, C. C., and Ramanathan, S., *J. Catal.* **184**, 535 (1999).
23. Delporte, P., Pham-Huu, C., and Ledoux, M. J., *Appl. Catal. A* **149**, 151 (1997).
24. Xiao, T.-C., York, A. P. E., Al-Megren, H., Claridge, J. B., Wang, H. T., and Green, M. L. H., *C. R. Acad. Sci. Paris, Ser. IIc* **3**, 451 (2000).
25. Bussell, M. E., Mills, P., Woodruff, B. P., Main, R., and Phillips, D. C., *Prepr.—Am. Chem. Soc. Div. Pet. Chem.* **44**, 206 (1999).
26. Topsoe, H., *Appl. Catal.* **25**, 273 (1986).
27. de Beer, V. H. J., Buchet, J. C., and Prins, R., *J. Catal.* **72**, 369 (1981).
28. Kim, D. W., Lee, D.-K., and Ihm, S.-K., *Catal. Lett.* **43**, 91 (1997).
29. Xiao, T. C., York, A. P. E., Williams, C. V., Al-Megren, H., Hanif, A., Zhou, X., and Green, M. L .H., *Chem. Mater.* **12**, 3896 (2000).
30. Smith, G. W., and Ibers, J. A., *Acta. Crystallogr.* **19**, 269 (1965).
31. Halawy, S. A., Mohamed, M. A., and Bond, G. C., *J. Chem. Technol. Biotechnol.* **58**, 237 (1993).
32. Mestl, G., and Srinivasan, T. K. K., *Catal. Rev.-Sci.Eng.* **40**, 451 (1998).
33. Ono, T., Ogata, N., and Miyaryo, Y., *J. Catal.* **161**, 78 (1996).
34. Claridge, J. B., York, A. P. E., Brungs, A. J., and Green M. L. H., *Chem. Mater.* **12**, 132 (2000).
35. Newsam, J. M., Jacobson, A. J., MaCandlish, L. E., and Polizzotti, R. S., *J. Solid State Chem.* **75**, 296 (1988).
36. Yu, C. C., Ramanathan, S., and Oyama, S. T., *J. Catal.* **173**, 1 (1998).